Dealiased spectral images from aliased Fizeau Fourier transform spectroscopy measurements

Samuel T. Thurman and James R. Fienup

The Institute of Optics, University of Rochester, Rochester, New York 14627, USA

Fizeau Fourier transform imaging spectroscopy (FTIS) is a technique for collecting both spatial and spectral information about an object with a Fizeau imaging interferometer and postprocessing. The technique possesses unconventional imaging properties due to the fact that the system transfer functions, including the imaging and spectral postprocessing operations, are given by cross correlations between subapertures of the optical system, in comparison with the conventional optical transfer function, which is given by the autocorrelation of the entire aperture of the system. The unconventional imaging properties of Fizeau FTIS can be exploited to form spatially dealiased spectral images from undersampled intensity measurements (obtain superresolution relative to the detector pixel spacing). We demonstrate this dealiasing technique through computer simulations and discuss the associated design and operational trade-offs. © 2006 Optical Society of America

OCIS codes: 070.2580, 100.3010, 100.3020, 100.6640, 110.5100, 120.6200.

1. INTRODUCTION

Fourier transform imaging spectroscopy[1–3] (FTIS) can be performed with an imaging Fizeau interferometer. One embodiment of a Fizeau interferometer is a multiple-telescope array. Figure 1 illustrates one such array having two telescopes or subapertures. For conventional imaging, optical delay lines are used to equalize the optical path length through each of the subapertures. Optical path differences (OPDs) between various subapertures can be introduced by adjustment of the delay lines. FTIS is performed by recording a sequence of panchromatic images with different OPDs between various groups of subapertures and Fourier transforming the measured fringe modulation at each image point. Spectral imagery resulting from this technique possesses some unconventional properties,[3] which present a challenging image reconstruction problem,[4] but also permit unique (additional) postprocessing opportunities. One example is the opportunity to form spatially dealiased spectral imagery from spatially aliased image measurements. This dealiasing provides imagery that is superresolved relative to the detector pixel spacing, but not relative to the diffraction limit. Note that this dealiaising technique is based on the specific imaging properties of Fizeau FTIS, in contrast to techniques based on subpixel dithering and the generalized sampling theorem.[5]

The reader is referred to Ref. 3 for a detailed analysis of the imaging properties of Fizeau FTIS. Here we summarize the equations of primary interest. Suppose the subapertures of a system are divided into Q groups, such that the generalized pupil function for the optical system can be expressed as

$$T_{\text{pup}}(\xi, \eta, \nu, \tau) = \sum_{q=1}^{Q} T_q(\xi, \eta, \nu) \exp(i 2\pi \nu \gamma_q \tau), \qquad (1)$$

where (ξ, η) are pupil coordinates, ν is the optical frequency ($= c/\lambda$ where c is the speed of light and λ is the wavelength), $\tau = \text{OPD}/c$ is a time-delay variable, $T_q(\xi, \eta, \nu)$ is the generalized pupil function for the qth subaperture group, and γ_q is a relative delay rate for the qth subaperture group. Note that the exponential term within the summation represents the phase differences introduced by the optical delay lines, which are linearly related. Also, without loss of generality, the subaperture groups are organized such that $\gamma_1 = 0$, $\gamma_{q+1} > \gamma_q$, and $\gamma_Q = 1$. In the limit that noiseless panchromatic image intensity measurements are made for all τ, the spectral image, $S_i(x, y, \nu')$, obtained by Fourier transforming the measured fringe modulation from τ to ν' is given by Eq. (8) of Ref. 3 as

$$S_i(x, y, \nu') = \sum_{\substack{p=1 \\ p \neq q}}^{Q} \sum_{q=1}^{Q} \int_{-\infty}^{\infty} \int_{-\infty}^{\infty} \frac{\kappa}{|\gamma_p - \gamma_q| M^2} S_o\left(\frac{x'}{M}, \frac{y'}{M}, \frac{\nu'}{\gamma_p - \gamma_q}\right)$$

$$\times h_{p,q}\left(x - x', y - y', \frac{\nu'}{\gamma_p - \gamma_q}\right) dx' dy', \qquad (2)$$

where $S_o(x, y, \nu)$ is the spectral density of the spatially incoherent object, $\kappa = \lambda^2/\pi$, M is the magnification of the imaging system, and $h_{p,q}(x, y, \nu)$ are spectral point spread functions (SPSFs), which correspond to spatial impulse response functions that result from conventional diffraction effects and the postprocessing Fourier transform from τ to ν'. The SPSFs are defined as

$$h_{p,q}(x, y, \nu) = t_p(x, y, \nu) t_q^*(x, y, \nu), \qquad (3)$$

where $t_q(x, y, \nu)$ is the conventional coherent impulse response for the subaperture pupil function $T_q(\xi, \eta, \nu)$ using Goodman's notation.[6] The appropriately normalized spatial Fourier transform of $h_{p,q}(x, y, \nu)$ is the spectral optical transfer function (SOTF) $H_{p,q}(f_x, f_y, \nu)$, which can be written in terms of the pupil functions $T_q(\xi, \eta, \nu)$ as
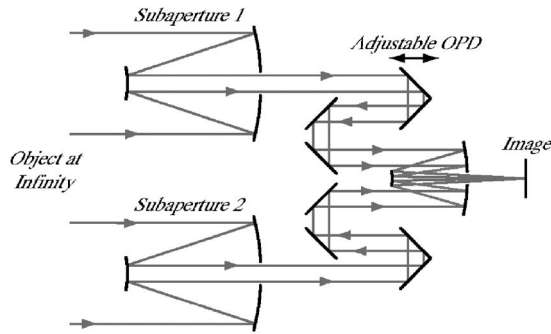
Fig. 1. Fizeau imaging interferometer composed of an array of two telescopes.

$$H_{p,q}(f_x,f_y,\nu) = \frac{1}{A_{\text{pup}}} T_p(-\lambda f_i f_x, -\lambda f_i f_y, \nu)$$

$$\star T_q(-\lambda f_i f_x, -\lambda f_i f_y, \nu), \qquad (4)$$

where f_i is the focal length of the imaging system and the symbol $\star$ represents a two-dimensional cross-correlation operator evaluated at $(-\lambda f_i f_x, -\lambda f_i f_y)$, where (f_x, f_y) are the spatial-frequency coordinates.

$$A_{\text{pup}} = \int_{-\infty}^{\infty} \int_{-\infty}^{\infty} |T_{\text{pup}}(\xi, \eta, \nu, 0)|^2 d\xi d\eta, \qquad (5)$$

where A_{pup} is the normalization constant for the conventional optical transfer function (OTF) given by

Unlike the conventional OTF, which is given by the autocorrelation of the entire pupil function, the SOTFs in Eq. (4) are given by cross correlations between subaperture-group pupil functions. The unconventional imaging properties of Fizeau FTIS result from this fact. For example, the cross correlation will vanish for vector separations less than the minimum separation between subaperture groups, which implies that the SOTFs will vanish at dc and in some neighborhood about the dc spatial frequency. The missing dc spatial frequencies cause $S_i(x,y,\nu')$ to be zero mean. The loss of low spatial frequencies means that $S_i(x,y,\nu')$ will be a bandpassed image of the object, with the signal being maximum at spatial edges in the scene. Furthermore, the cross-correlation operation permits SOTFs that are non-Hermitian with respect to the dc spatial frequency, which implies that $S_i(x,y,\nu')$ will be complex valued in general. Of specific interest to this work is the fact that the SOTFs can have asymmetric regions of support, which is the basis for the dealiasing technique that is described here. For a more extensive discussion of the imaging properties of Fizeau FTIS, the reader is referred to Ref. 3.

In Section 2, we describe the dealiasing principle. Section 3 contains a discussion of the design and operational trade-offs associated with the dealiasing technique. Example results from a computer simulation demonstrating the technique are presented in Section 4. Section 5 contains some concluding remarks.

2. DEALIASING PRINCIPLE
The dealiasing principle is based on exploiting the unconventional imaging properties of Fizeau FTIS. Suppose the

SOTFs have asymmetric support regions such that, when they are spatially aliased, the aliased portions of the support regions do not overlap with the unaliased support regions. In such a case, the aliased spatial-frequency content of $S_i(x,y,\nu')$ will not be corrupted by unaliased low spatial-frequency content. Thus a dealiased spectral image, $S_d(x,y,\nu')$, can be formed directly from $S_i(x,y,\nu')$ and knowledge of the SOTF terms by a remapping in the spatial-frequency domain. The simulation results in Section 4 illustrate a practical method for performing the dealiasing.

3. DESIGN AND OPERATIONAL TRADE-OFFS
The most fundamental design trade-off is that the arrangement of subapertures within the pupil of the optical system needs to be conducive to forming asymmetric SOTF terms with small regions of support, which facilitates dealiasing. Figure 2 shows three subaperture arrangements. While each subaperture arrangement may be favorable for ordinary FTIS operation, the first two are unfavorable for the dealiasing technique. The arrangement in Fig. 2(a) yields SOTFs that have symmetric support regions; for larger detector pixels there would be an overlap of the aliased SOTFs in both the horizontal and vertical dimensions, preventing the separation of the aliased and unaliased terms. The arrangement in Fig. 2(c) yields SOTFs with supports that are considerably broader in the vertical dimension than the horizontal dimension, and the aliased SOTFs will overlap in the vertical direction for larger pixels. By reducing just the vertical dimension of the subapertures in Fig. 2(c) by a factor of 2, the subaperture arrangement can be made favorable for the dealiasing technique to work in the horizontal direction, as shown in Figs. 2(e) and 2(f). An example of a favorable subaperture arrangement is given in Section 4.

Given a fixed subaperture arrangement, there are operational trade-offs that can be used to facilitate the dealiasing technique. The operational trade-off that we will consider is to perform multiplexed Fizeau FTIS by dividing the system subapertures into $Q > 2$ groups. Because this technique involves the simultaneous introduction of different OPDs between different baselines in the system, the data collection is operationally more complex. Additional trade-offs associated with multiplexed FTIS are: (i) the spectral bandwidth of the image must be limited, e.g., with a color filter, to permit demultiplexing of the data [need $(\nu_{\max} - \nu_{\min})/\nu_{\max} \leqslant 1/3$ for $Q=3$ groups], and (ii) the spectral resolution of the demultiplexed data will vary depending on the maximum OPD introduced between each group of subapertures, thereby yielding different spectral resolution for different spatial frequencies when $Q > 2$.[3] However, multiplexed FTIS can yield individual SOTFs with smaller individual support regions, by appropriate selection of the subaperture groups. Additionally, the combined support of the SOTFs for multiplexed $(Q > 2)$ FTIS can be larger than that for the case of $Q=2$, which translates into the collection of spectral data over a larger region of spatial frequencies. Reference 3 contains a more detailed discussion of trade-offs associated with multiplexed FTIS.
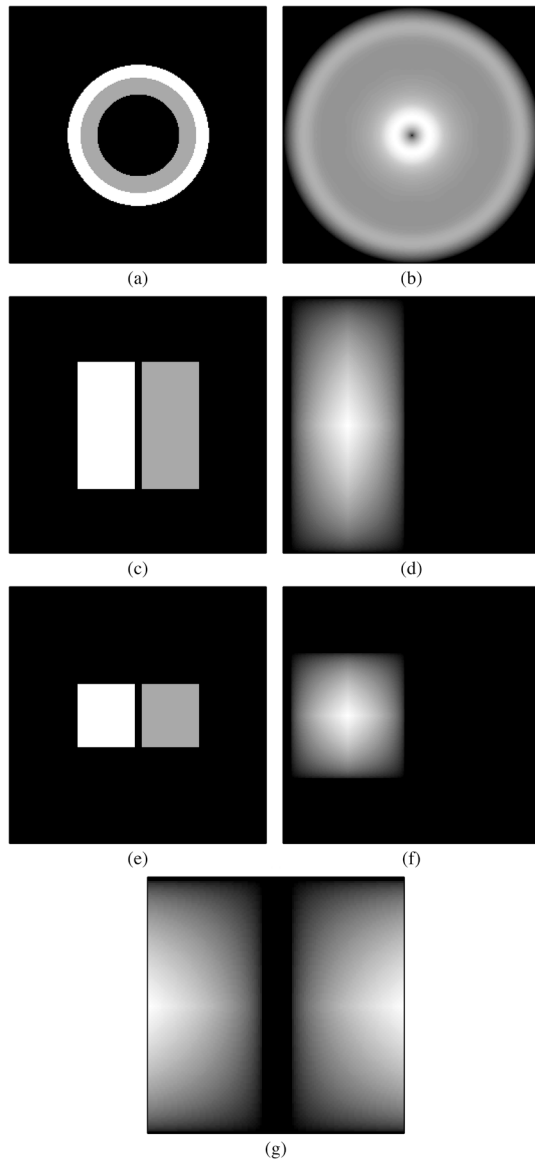
Fig. 2. Example pupil arrangements: (a) two concentric annular subapertures, where the different subapertures are indicated by shading, and (b) corresponding SOTF; (c) two rectangular subapertures and (d) corresponding SOTF; (e) two square subapertures and (f) corresponding SOTF; and (g) aliased version of the SOTF shown in (f).

The main benefit of the dealiasing technique is the ability to use a detector with larger pixels, while retaining fine spatial resolution. Larger detector pixels translate into a signal-to-noise ratio boost and a wider field of view for a fixed number of detector pixels.

4. SIMULATION EXAMPLE

A. Aliased Intensity Measurements

Figure 3 shows the pupil configuration of the optical system modeled in the computer simulation, where shading is used to indicate the subaperture groups. The relative delay rates for the subaperture groups were $\gamma_1 = 0$, $\gamma_2 = 1/3$, and $\gamma_3 = 1$. Tables 1 and 2 list additional optical system and detector parameters used in the simulation. The

simulation used a synthetic hyperspectral scene generated by the Digital Imaging and Remote Sensing Image Generation[7] (DIRSIG) model for the object spectral radiance in units of $[\mu W\,cm^{-2}\,sr^{-1}\,Hz^{-1}]$. The scene is a nadir view of a water treatment plant from the top of the atmosphere with 256×256 spatial samples at a ground sample spacing of $\Delta x = \Delta y = 1$ ft. The scene is spectrally band limited to the optical frequencies $\nu = 319 - 400$ THz ($\lambda = 0.75 - 0.94\,\mu m$), with 90 spectral samples at a sample spacing of $\Delta \nu = 0.90$ THz.

The pixel pitch, $\Lambda_{Nyquist}$, required for Nyquist sampling of the intensity is given by[8]

$$\Lambda_{Nyquist} = \frac{\min(\lambda)f_i}{2D} = 11.25\,\mu m \qquad (6)$$

(assumed to be the same in both dimensions), but the dealiasing technique allows the use of a detector with a coarser pixel pitch. Figure 4 shows both unaliased and
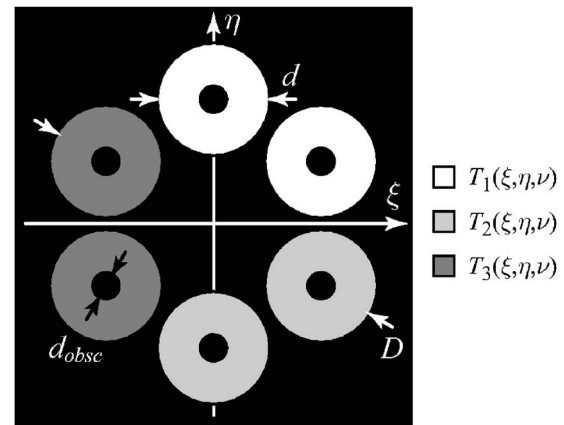

Fig. 3. Pupil configuration used for computer simulation. The subaperture group pupil functions, $T_q(\xi, \eta, \nu)$ for $q = 1$, 2, and 3, are indicated by shading.

Table 1. Optical System Parameters for Simulation

D	1.60 m
d	0.50 m
d_{obsc}	0.10 m
F-number	30
Effective focal length, f_i	48 m
Optical efficiency, η_i	85%
Image space solid angle, Ω_i	4.91×10^{-4} sr

Table 2. Detector Parameters for Simulation

Pixel pitch, Λ_{det}	22.5 μm
Fill factor, f_{det}	95%
Quantum efficiency,[a] η_{det}	85%
Well depth	40,000 e^{-b}
Dark current, i_{dark}	1 e$^-$/sec
Read noise, σ_{det}	20 e$^-$
A/D converter gain, g_{det}	10 e$^-$/count
A/D converter bits	12
Exposure time, t_{det}	2 msec

[a]Assumed to be uniform over the spectral bandwidth of the image.

[b]e$^-$ represents a detected photoelectron.
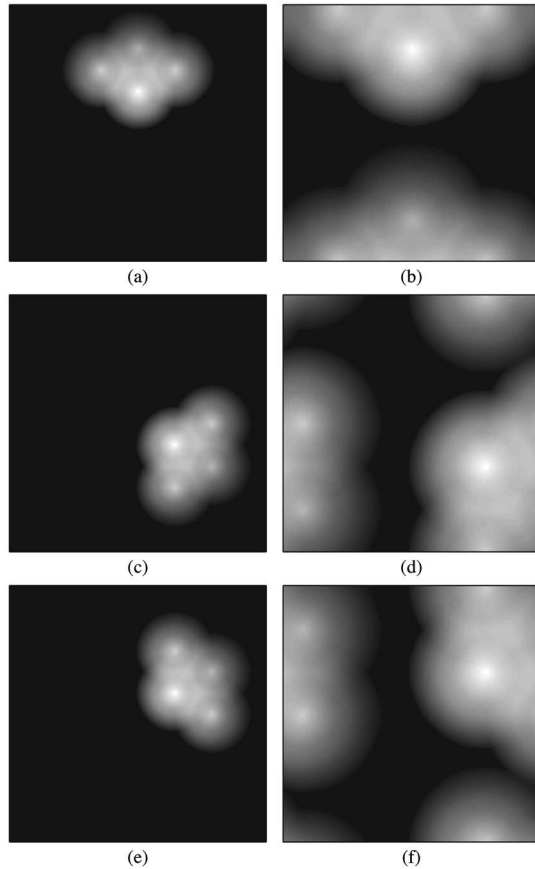
Fig. 4. SOTFs corresponding to the pupil configuration of Fig. 3: (a), (c), and (e) show unaliased (11.25 μm detector sample spacing) versions of $H_{2,1}(f_x,f_y,\nu_0)$, $H_{3,2}(f_x,f_y,\nu_0)$, and $H_{3,1}(f_x,f_y,\nu_0)$, respectively, and (b), (d), and (f) show aliased (22.5 μm detector sample spacing) versions of the same SOTFs, for $\nu_0=387$ THz.
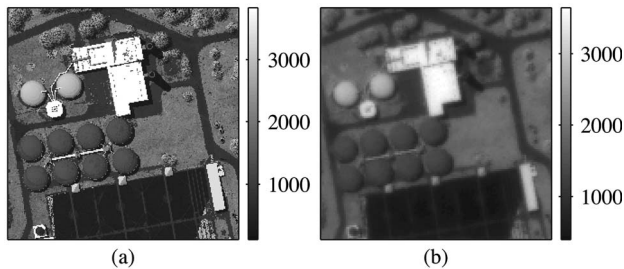

Fig. 5. Data from simulation: (a) panchromatic view of the DIRSIG scene used for the object (scaled to units of detector counts) and (b) simulated image measurement for $\tau=0$.

aliased versions of the SOTFs, $H_{p,q}(f_x,f_y,\nu)$, for the simulation. The unaliased SOTFs correspond to a sample spacing of $\Lambda_{\mathrm{Nyquist}}=11.25$ μm in the image plane, while the aliased SOTFs correspond to a sample spacing of $\Lambda_{\mathrm{det}}=22.5$ μm in the image plane. Note that the support of each aliased SOTF is asymmetric, such that there is no overlap between the aliased and unaliased portions of each SOTF for a sample spacing of 22.5 μm; that is, the aliased values are uncorrupted. The dealiasing is based on this property of the SOTFs.

A set of aliased intensity measurement was generated by passing a 256×256 unaliased intensity pattern with a

sample spacing of 11.25 μm through the detector transfer function, $H_{\mathrm{det}}(f_x,f_y)$, and then downsampling by a factor of 2, resulting in an aliased intensity pattern with 128 $\times128$ spatial dimensions and a sample spacing of 22.5 μm. Assuming square detector pixels,

$$H_{\mathrm{det}}(f_x,f_y) = \mathrm{sinc}(\Lambda_{\mathrm{det}}\sqrt{f_{\mathrm{det}}}f_x)\mathrm{sinc}(\Lambda_{\mathrm{det}}\sqrt{f_{\mathrm{det}}}f_y). \tag{7}$$

Noise was included in the simulated measurements by: (i) calculating the expected value of detected photoelectrons for each panchromatic image, (ii) adding the expected value of photoelectrons due to dark current, (iii) using a Poisson random number generator to produce a realization of the number of detected photoelectrons, (iv) adding zero-mean Gaussian noise with a standard deviation of σ_{det} to simulate detector read noise, (v) converting the signal to units of detector counts by dividing by the A/D converter gain, and (vi) quantizing the detector count signal to integer numbers. The exposure time for each frame, t_{det}, was chosen to avoid saturating the detector. A total of 256 panchromatic image measurements were simulated for uniformly spaced time delays over the range $\tau=-134.5$ to $+133.4$ fs with a sample spacing of $\Delta\tau=1.05$ fs, equivalent to an OPD of $c\Delta\tau=0.315$ μm. Figure 5 shows a panchromatic view of the DIRSIG scene and the simulated image measurement for $\tau=0$ fs.
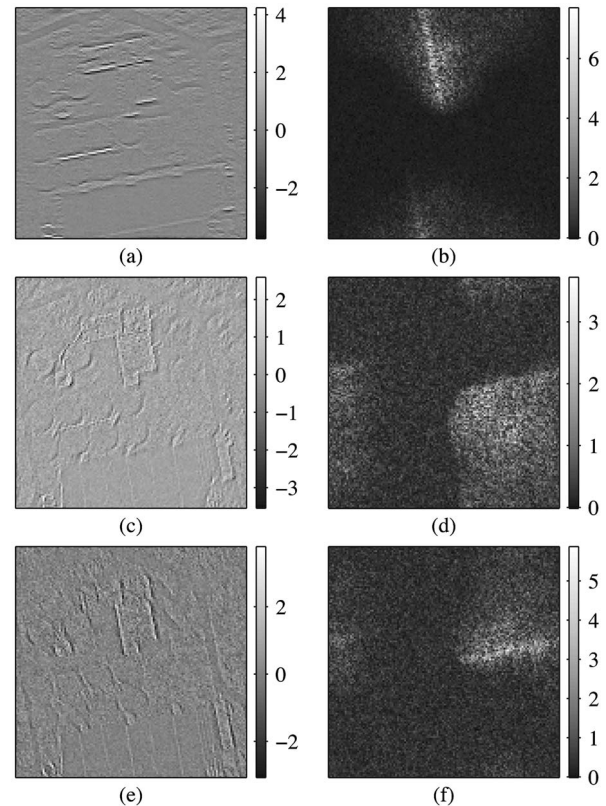

Fig. 6. Aliased spectral imagery from simulation: the real part of the complex-valued spectral image $S_i(x,y,\nu)$ for (a) $\nu=\nu_0/3$, (c) $\nu=2\nu_0/3$, and (e) $\nu=\nu_0$, and (b), (d), and (f) the corresponding Fourier magnitude of each of the complex-valued images represented in the left column, for $\nu_0=387$ THz. The corresponding SOTFs are shown in Figs. 4(b), 4(d), and 4(f).
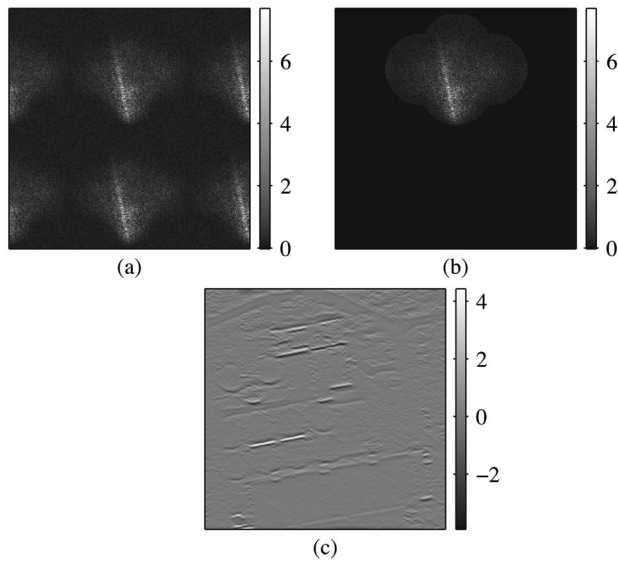
Fig. 7. Illustration of the dealiasing procedure: (a) tile the aliased spatial-frequency data, $G_i(f_x, f_y, \nu)$, forming a data set with 256×256 spatial-frequency dimensions from the 128×128 aliased data set; (b) band limit the tiled spatial-frequency data to the support of the corresponding SOTF to form $G_d(f_x, f_y, \nu)$, the dealiased spatial-frequency data; and (c) inverse Fourier transform to yield the dealiased spectral image $S_d(x, y, \nu)$. The data shown in this figure correspond to $\nu = \nu_0/3$. Thus Fig. 7(c) is the dealiased version of Fig. 6(a).
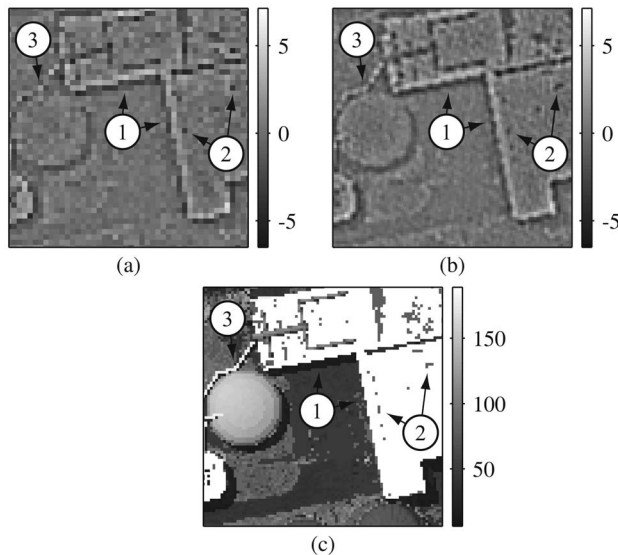

Fig. 8. Comparison of magnified portions of the composite spectral imagery with the object data for $\nu = \nu_0$: (a) real part of aliased composite spectral image, (b) real part of dealiased composite spectral image, and (c) object truth data. The arrows point to specific features that are discussed in the text.

B. Dealiasing Procedure

The spectral image $S_i(x, y, \nu')$ is obtained from the intensity measurements by Fourier transforming the measured fringe modulation at each detector pixel (x, y) from τ to ν' space. This operation also demultiplexes the spectral information associated with the different OPDs introduced between each pair of supaperture groups during data collection. Figure 6 shows the demultiplexed spectral

imagery corresponding to a particular optical frequency, $\nu_0 = 387$ THz, as well as $|G_i(f_x, f_y, \nu)|$, the magnitude of the spatial Fourier transform of $S_i(x, y, \nu)$, for each of three SOTF terms. In the spatial-frequency domain, note that the signal within $G_i(f_x, f_y, \nu)$ is confined to the support of the corresponding SOTFs, shown in Figs. 4(b), 4(d), and 4(f), whereas the noise is spread uniformly over the entire spatial-frequency domain. Also, notice that the aliased spatial-frequency information is not corrupted by the unaliased spatial frequencies of the image. Dealiasing is performed by rearranging the Fourier data to put it at its true spatial frequencies. A straightforward procedure for forming a dealiased spectral image $S_d(x, y, \nu)$ is illustrated in Fig. 7. For each SOTF term, $G_i(f_x, f_y, \nu)$ is tiled along the spatial-frequency directions and then band limited to the support of the corresponding SOTF to form $G_d(f_x, f_y, \nu)$. Then the inverse spatial Fourier transform is taken to yield the dealiased spectral image $S_d(x, y, \nu)$.

Each demultiplexed component of the spectral imagery contains unique spatial-frequency information because each component has a different SOTF. The demultiplexed data can be combined to form a composite spectral image with the combined spatial-frequency content of all of the demultiplexed components, using Eq. (10) of Ref. 3. Figure 8 shows magnified portions of the aliased and dealiased spectral images and the object data for $\nu = \nu_0$. Notice that the building edges (1) are sharper in the dealiased image than they are in the aliased image. Also, the features on the building roof (2) are better represented in the dealiased image than in the aliased image. Specifically, the elongated features appear pointlike in the aliased image and elongated in the dealiased image. Further, the pipelike object (3) is more easily recognizable in the dealiased image than it is in the aliased image.

C. Image Reconstruction

One consequence of the SOTFs being the cross correlations between subaperture pupil functions is that the
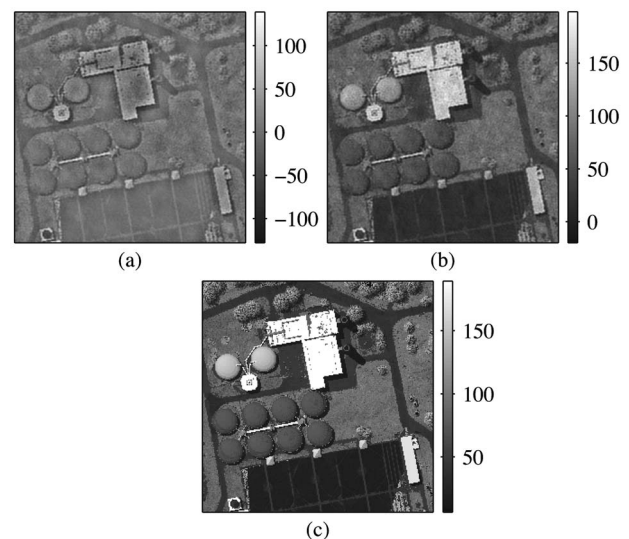

Fig. 9. Comparison of reconstructed spectral imagery with the object data for $\nu = \nu_0$: (a) linear Wiener–Helstrom reconstruction, (b) nonlinear reconstruction using the algorithm from Ref. 4 and (c) object truth data.
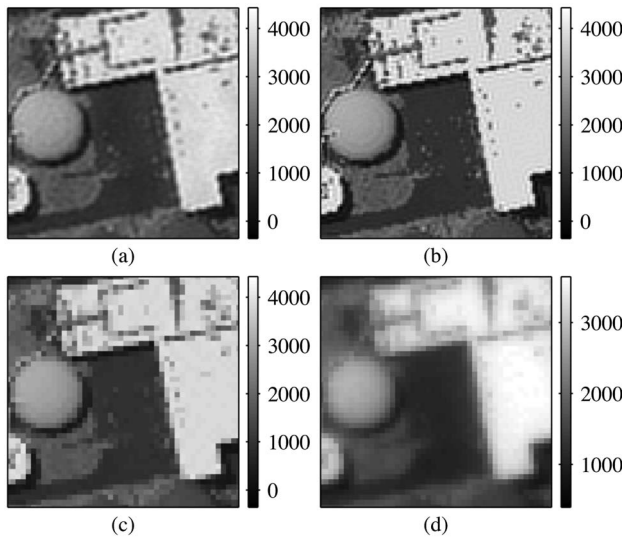
Fig. 10.   Panchromatic views of (a) nonlinear reconstruction of the spectral image, (b) object truth data band limited to spatial frequencies passed by the conventional OTF, (c) aliased version of (b), and (d) raw $\tau=0$ image.

SOTFs vanish necessarily in a finite region about the dc spatial frequency for nonoverlapping pupil functions. Thus a finite area of low spatial frequencies is missing from the spectral imagery, which cannot be reconstructed by a linear algorithm like a Wiener–Helstrom filter.[9] Reference 4 describes a nonlinear algorithm for reconstructing these missing low spatial frequencies from the panchromatic intensity measurements, using the statistical properties of natural scenery. Figure 9 shows both a Wiener–Helstrom reconstruction of the spectral image and the results of using the nonlinear algorithm from Ref. 4. Notice that the Wiener–Helstrom filter sharpens edges in the scene, but the nonlinear algorithm is required for reconstructing the missing low spatial frequencies. Finally, over a zoomed-in area, Fig. 10 shows panchromatic views of the nonlinear reconstruction and the object truth, band limited to spatial frequencies passed by the conventional OTF. Notice that the fine detail in the reconstruction from the dealiased spectral imagery is real.

5. CONCLUSIONS

Fizeau FTIS has unconventional imaging properties due to the fact that the imaging transfer functions for the resulting spectral imagery, the SOTFs, are given by the cross correlations between pupil functions for different subaperture groups. This unusual property presents some technical challenges, but also provides unique postpro-

cessing opportunities. The ability to form dealiased spectral imagery from spatially aliased intensity measurements is one example of such an opportunity. This technique is based on the fact that the SOTFs associated with Fizeau FTIS can be asymmetric. Certain design and operational trade-offs must be met as described in Section 3, including aperture arrangements and spectral bandwidth and resolution considerations. The main advantage of the technique is that it allows a system to operate with a detector having larger pixels while retaining fine spatial resolution, which yields an increased signal-to-noise ratio and an increased field of view for a fixed number of detector pixels. The simulation example demonstrates a straightforward procedure for implementing the technique.

Portions of this paper were presented in Ref. 10.

ACKNOWLEDGMENTS

Corresponding author S. Thurman may be reached by e-mail at thurman@optics.rochester.edu.

REFERENCES

1. M. Frayman and J. A. Jamieson, "Scene imaging and spectroscopy using a spatial spectral interferometer," in *Amplitude and Intensity Spatial Interferometry*, J. B. Breckingridge, ed., Proc. SPIE **1237**, 585–603 (1990).
2. R. L. Kendrick, E. H. Smith, and A. L. Duncan, "Imaging Fourier transform spectrometry with a Fizeau interferometer," in *Interferometry in Space*, M. Shao, ed., Proc. SPIE **4852**, 657–662 (2003).
3. S. T. Thurman and J. R. Fienup, "Multi-aperture Fourier transform imaging spectroscopy: theory and imaging properties," Opt. Express **13**, 2160–2175 (2005), http://www.opticsexpress.org/abstract.cfm?URI=OPEX-13-6-2160.
4. S. T. Thurman and J. R. Fienup, "Fizeau Fourier transform imaging spectroscopy: direct nonlinear image reconstruction" (submitted to Opt. Express).
5. A. Papoulis, "Generalized sampling expansion," IEEE Trans. Circuits Syst. **24**, 652–654 (1977).
6. J. Goodman, *Introduction to Fourier Optics*, 3rd ed. (Roberts & Co., 2004).
7. J. Schott, *Remote Sensing: The Image Chain Approach* (Oxford, 1996).
8. R. D. Fiete, "Image quality and $\lambda FN/p$ for remote sensing systems," Opt. Eng. **38**, 1229–1240 (1999).
9. C. W. Helstrom, "Image restoration by the method of least squares," J. Opt. Soc. Am. **57**, 297–303 (1967).
10. S. T. Thurman and J. R. Fienup, "Dealiased spectral images from aliased Fizeau Fourier transform imaging spectroscopy measurements," in *Frontiers in Optics/Laser Science XXI* (Optical Society of America, 2005), paper FTuM2.